AIMS Geosciences

AIMS Geosciences, 4 (1): 1–20.
DOI: 10.3934/geosci.2018.1.1
Received: 20 October 2017
Accepted: 12 February 2018
Published: 12 March 2018

http://www.aimspress.com/journal/geosciences

Research article

Rayleigh wave group velocity model of the southeast flank of the Rio Grande Rift using Cross-Correlation

Luis M. Sandoval*, Philip C. Goodell, Hector Gonzalez-Huizar and Munazzam Ali Mahar

Department of Geological Sciences, University of Texas at El Paso, El Paso, Texas, 79968, USA

*** Correspondence:** Email: lsandoval@miners.utep.edu.

Abstract: The southeast shoulder of the Rio Grande Rift is located in southeastern New Mexico and west Texas in US and northern Chihuahua in Mexico. Noted mineral resources in the region are enriched in rare earth elements increasing the interest of research. These resources are related to tertiary volcanism. The magmas of this volcanism have similar composition of that of the oceanic island basalts suggesting that they were created from asthenosphere derived magmas from the basement of the North American Craton. That basement, in the area of interest, constitutes the Mazatzal and Grenville Proterozoic provinces of the Proterozoic Laurentia plate. This study is intended to contribute to the general understanding of the basement features of the region. In order to understand the structure of the crust and upper mantle we create a Rayleigh surface wave group velocity model of the southeast flank (or shoulder) of the Rio Grande Rift. Rayleigh wave group velocities were calculated using data from EarthScope's TA and Flex arrays. The periods of the model range from 10 s to 160 s. The kernels of the model are taken from the joint inversions made for LA RISTRA, from where the depths corresponding to periods between 10 s to 160 s should be approximately between 10 km and 350 km of depth. The results show the anisotropy of the region and difficulties faced using the Rayleigh wave cross correlation. Some structures like the Delaware basin are complicated and sensitive to seismic radiation directions and patterns. In general, structures are better resolved when these radiation directions are perpendicular to the structure boundaries.

Keywords: Rayleigh wave; cross correlation; dispersion curves; East Flank Rio Grande Rift; Mazatzal; Grenville

1. Introduction

The location of interest is the southeast shoulder of the Rio Grande Rift on the boundary between southeast New Mexico and west Texas in the southwest of USA (Figure 1). This shoulder constitutes the west margin of the Great Plains; it is at the southwestern part of the North American Craton [1,2].

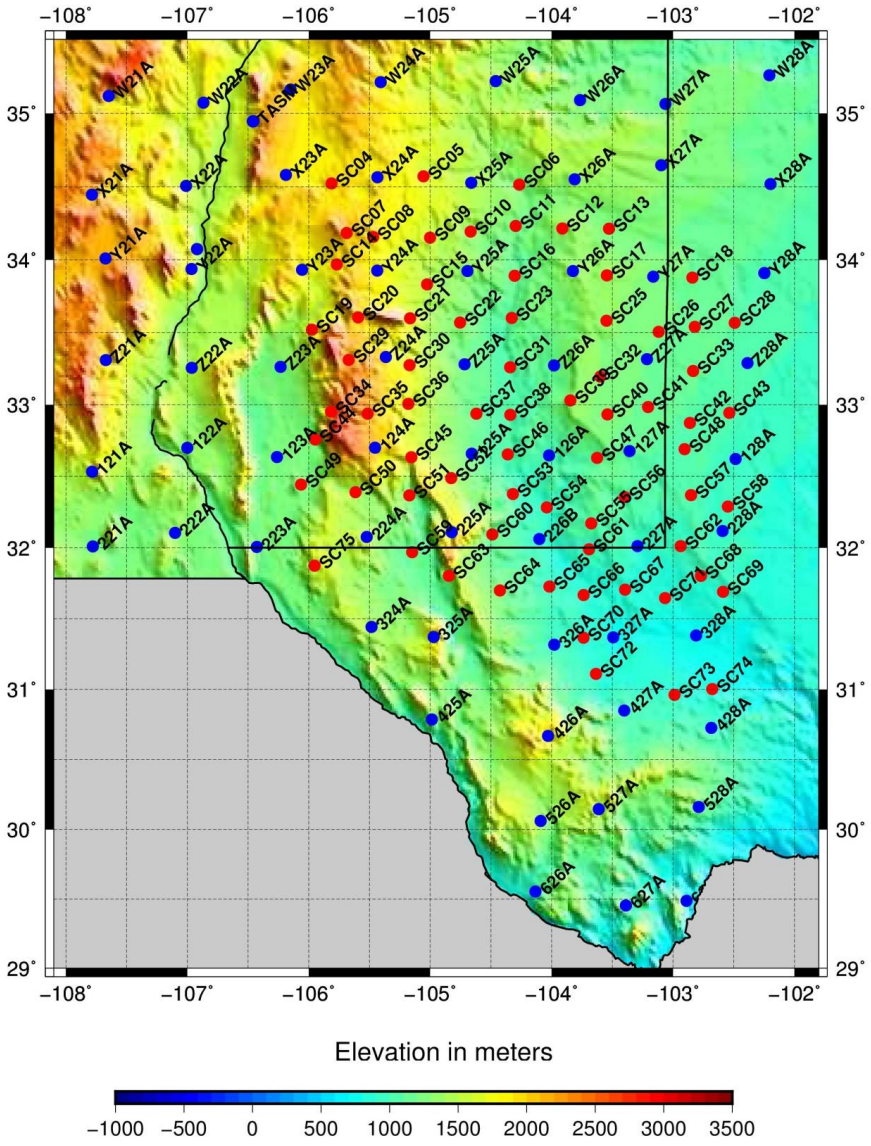

Figure 1. The stations deployed by USArray in the region; the blue dots represent the stations of the TA array and the red dots represent the stations of the XR array.

The basement of the North American Craton is the Proterozoic Laurentia plate. Southwestern Laurentia constitutes the Mojave, Yavapai, Mazatzal and Grenville Precambrian provinces, ordered by age and located from northwest to southeast [3]. The basement of this region is the source of extensive geological, geophysical and geochemical research, but it remains poorly understood [3–9]. The fact that it is mostly covered with younger formations and located in the boundary between two countries (Mexico and USA) have contributed to the problem.

Mineral resources found in this region include rare earth elements, beryllium and molybdenum related to Tertiary igneous activity. Ignimbrites related to the large silicic event that constitutes the

Sierra Madre Occidental are present in calderas at west Texas; some examples are Quitman, Eagle and Chinati [10–14]. Laccoliths are located at places such as Cornudas and Sierra Blanca, TX; stratovolcanoes such as Sierra Blanca, NM and the batholith at Capitan in New Mexico, also contain anomalously high concentrations of incompatible elements [12,15–17]. The magmas that created these igneous features rich in rare earth elements, beryllium and molybdenum have similar tholeiitic and alkalic composition to those of oceanic-island basalts indicating the possibility of having originated as asthenosphere derived melts in the lithospheric mantle during extension [18].

2. Data background

The seismic data used in this study is the Broad-band High-gain Z-component (BHZ) of the seismograms registered by two seismic projects: The transportable array (TA) [19] and the Flex array (XR) [6,20,21]. Both projects were deployed by EarthScope USArray, supported by National Science Foundation (NSF) and are available for download at the official website of the Incorporated Research Institutions for Seismology, IRIS [22]. We use the WILBER3 tool to download the data [23]. The distribution of the seismic stations is listed in Appendices 1 and Appendices 2, and shown in Figure 1. Three events were specially selected to make the analysis: The first was a magnitude 6.4 earthquake off the coast of Jalisco Mexico (17.52° N, 105.46° W) on September 24, 2008; 02: 33: 05 UTC. The second was a magnitude 6.5 earthquake off the coast of Northern California (40.67° N, 124.47° W) on January 10, 2010; 00: 27: 41 UTC. The third was a magnitude 8.1 earthquake in the Samoa Islands Region (15.5119° S, 171.9369° W) on September 29, 2009; 17: 48: 11 UTC. The time window was considered to select the events; the TA array stations were deployed in the area of interest approximately from February 2008 to February 2010; and the Flex array from August 2008 to December 2011. The events were selected based on large event magnitude and teleseismic distances to produce the best amplitude and signal to noise ratio to model the crustal structure [24]. Large Rayleigh wave amplitudes, relatively low attenuations and long propagation paths have contributed significantly to our understanding of the seismotectonics in the region [25]. The frequent occurrence of earthquakes and growing number of seismic stations near the southeast flank of the Rio Grande Rift made possible the study of the area's Rayleigh wave group velocities. This procedure was selected because it allows the collection with relative ease of a dense distribution of paths using stations within or near the area of research [25, 26]. The results shed new light on the seismotectonics of the region.

The geodetic model and isostatic residual gravity anomaly data were downloaded from USGS Mineral Resources On-Line Spatial Data's website [27]. In Figure 6, the contour of the zero isostatic anomaly is shown for reference [28, 29]. Shore lines and borderlines are provided by Generic Mapping Tools, GMT [30, 31]. The Elevation Model (ETOPO 1) was downloaded from National Oceanic and Atmospheric Administration's National Centers for Environmental Information, NOAA's NCEI [32].

3. Methodology

The following procedure is based on cross correlation of filtered surface waves in to specific band-widths to approximate the inter-station empirical Green's functions using inter-station

surface wave dispersion curves. This work was performed using transient seismic signals of the three specific events mentioned in the data section [24,33–36].

The selected data was processed using the Seismic Analysis Code (SAC) developed by B. Savage and A. Snoke and provided also by IRIS [37,38]. The distance, longitude and latitude of the event and the seismic stations are read from the header of the seismograms. The travel time of the group is calculated using cross correlation. No removal of instrument contribution was necessary because the data was obtained with identical instruments (Streckeisen STS-2 G3 coupled with Quanterra 330 Linear Phase), so they have the same response and same sensitivity; they are also calibrated under the same criteria because they were all deployed by USArray under the same project, EarthScope [21].

The distance between two stations is measured by the subtraction of the great circle path lengths connecting the event with the two stations. In this procedure we also use ray tracing, illustrated in Figures 2a, 2b and 2c, to choose the specific pair of stations; it elucidates the relative position and the order of the stations. The first station should be near, or directly on the seismic path between the event and the second station.

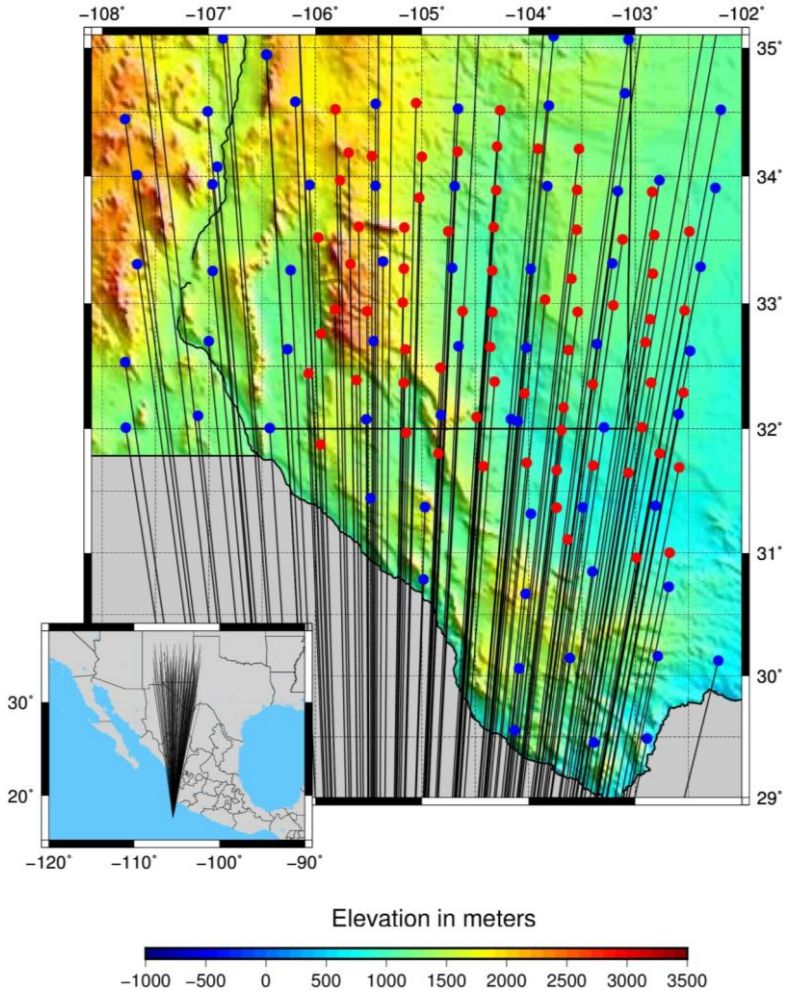

Figure 2a. Ray tracing of the events in Jalisco. Blue dots represent stations of TA array and red dots represent stations of XR array. The background colors represent elevation in meters over sea level.

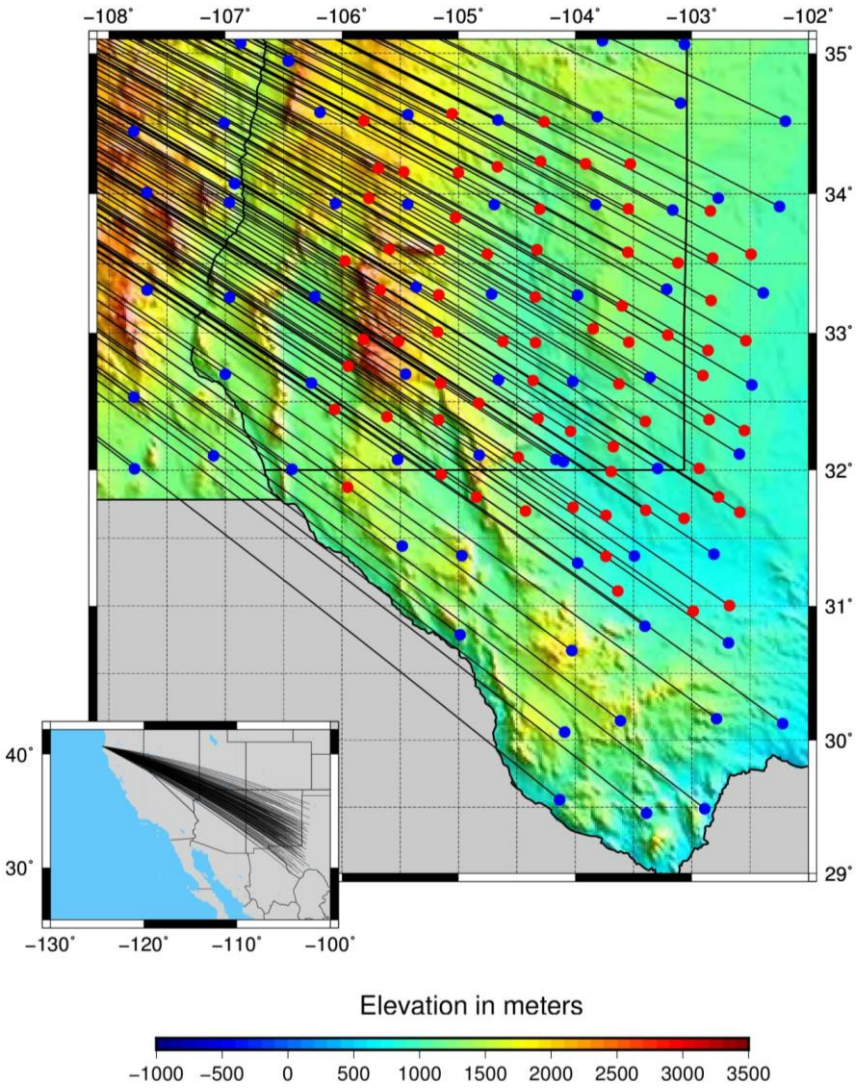

Figure 2b. Ray tracing of the event in California. Blue dots represent stations of TA array and red dots represent stations of XR array. The background colors represent elevation in meters over sea level.

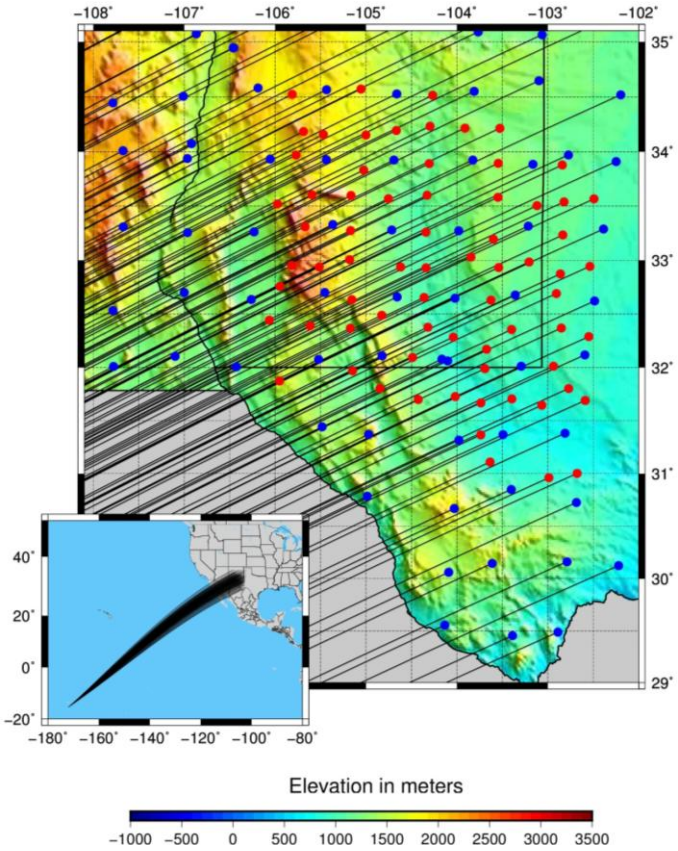

Figure 2c. Ray tracing of the event in Samoa. Blue dots represent stations of TA array and red dots represent stations of XR array. The background colors represent elevation in meters over sea level.

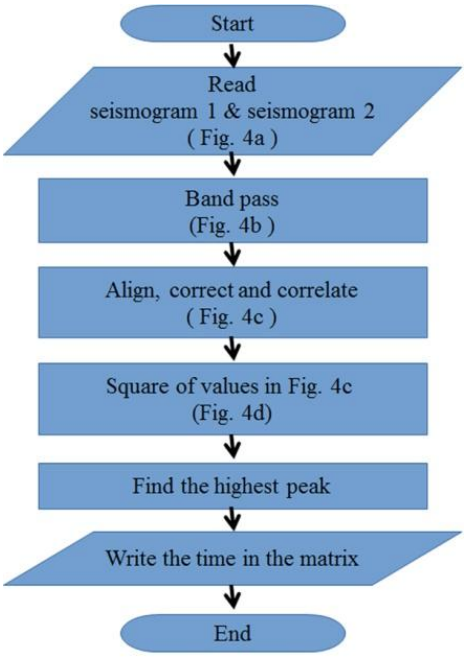

Figure 3. This procedure was coded in SAC to obtain the correlation times.

Now that the two stations are identified to be along similar paths and the distance between the two stations is calculated, the seismic travel time between the first and the second station is then calculated using cross correlation. To achieve the cross correlation, the seismograms are loaded into SAC and filtered in the desired frequency band with a specific ban-width. Once the filtering is done, the output signal is corrected and cross-correlated to measure the difference in arrival times; Figure 3 and Figure 4 describe the process graphically [33,34,36].

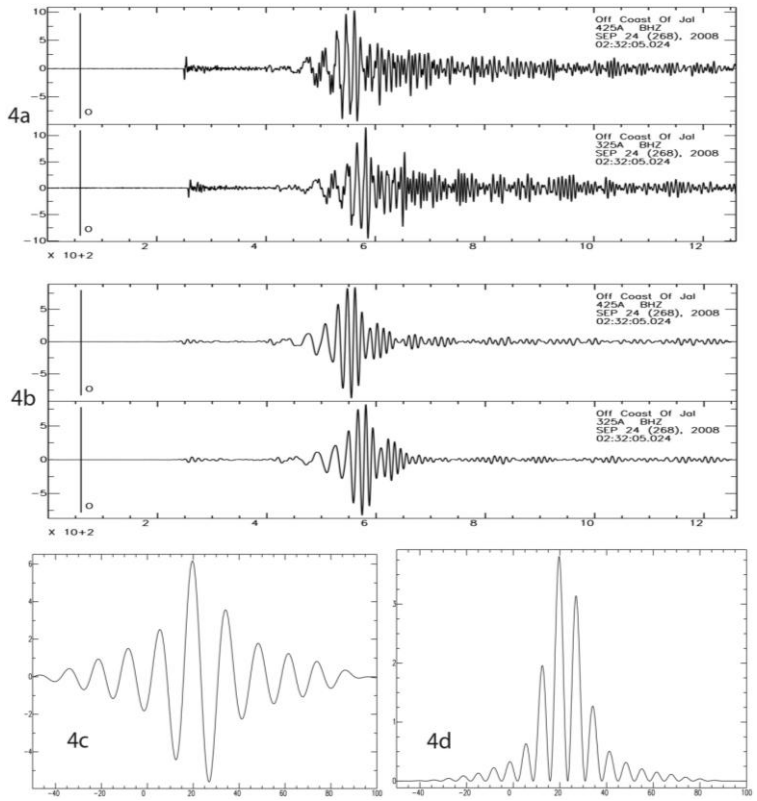

Figure 4. Seismograms of an event off the coast of Jalisco. 4a: Are the rough seismograms; 4b: are the seismograms after filtered; 4c: the cross correlation; 4d: the square of the cross correlation. The x axis is in seconds and the y axis is relative amplitude.

The filter is a band-pass Butterworth order six [39,40]. It is applied twice with the desired corners from where we define the group. After the correlation the signal is squared to facilitate the identification of the largest peak (maximum). Note that in Figure 4d the maximum amplitude is seen approximately at 19 seconds. The average velocity is then calculated as the ratio between the difference in distance and the correlation time.

We follow the same process for different groups spanning the frequencies available from the seismograms; in this part of the process the physical characteristics of the instrument establish the limitations (Nyquist is 20 Hz). The seismic average velocities of the group are plotted versus period to generate the dispersion curves (Figure 5a).

The seismograms were filtered at different band-widths with initial period of 10 seconds. The frequency bandwidths span at increments corresponding to multiples of 5/10, 6/10, 7/10 and 8/10 [33,36]. Figure 5a shows dispersion curves for the stations listed with frequency limits and bandwidths

calculated for the event in Jalisco. These dispersion curves and the blockmean tool of the GMT software provided the data to make the profile shown in Figure 5b. The approximate depths labeled in the plot of the dispersion curves in Figure 5a and the profile in Figure 5b on their right axes were taken from the inversion of the model ak135 [41,42]. The red dots in the profile of Figure 5b represent the depth of the Moho according to the receiver functions of the EarthScope Automated Receiver Survey, EARS [43].

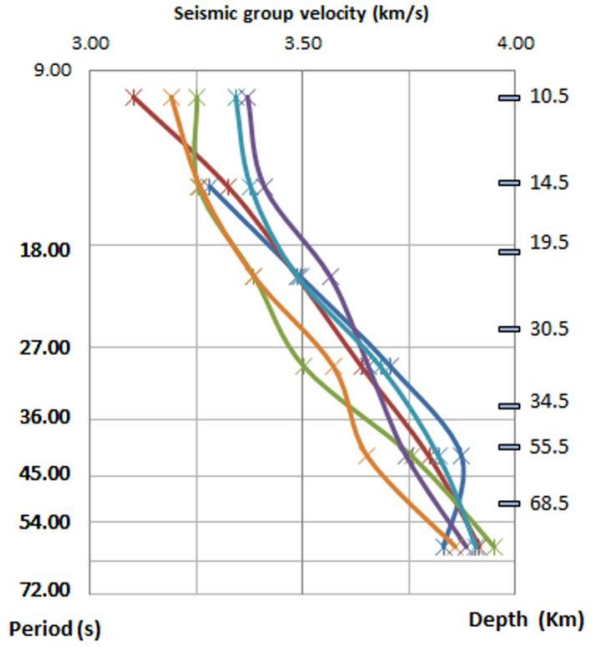

From Station	To Station	Line & Pair
TA-223A	TA-123A	l3p1
TA-123A	TA-Z23A	l3p2
TA-Z23A	TA-Y23A	l3p3
TA-Y23A	TA-X23A	l3p4
TA-X23A	TA-W23A	l3p5
TA-W23A	TA-V23A	l3p6

Group	From Period (s)	To Period (s)	Bandwidth Period (s)
1	10.00	14.29	4.29
2	14.29	20.41	6.12
3	20.41	29.15	8.75
4	29.15	41.65	12.49
5	41.65	59.50	17.85
6	59.50	85.00	25.50

Figure 5a. Dispersion curves for the event in Jalisco. Horizontal axis represents speed in km/s, the vertical axes, on the left, represents the period in seconds and on the right, represents the approximate depths according to ak135. The line runs from station TA-223A to station TA-W23A approximately from 32° to 35° latitude along −106.25° longitude. Please see Figure 1 to identify the stations involved in the pairs along the line 3.

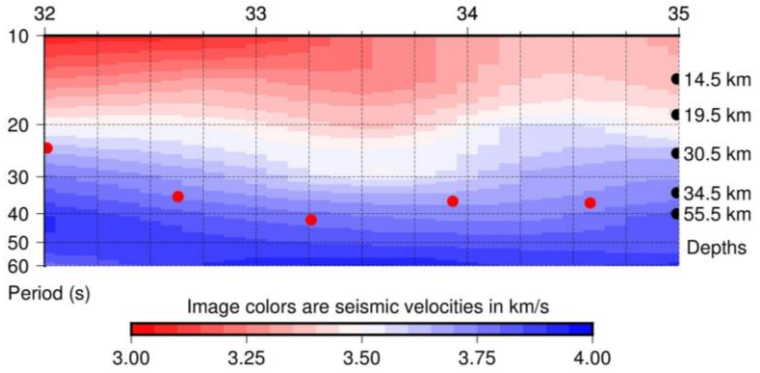

Figure 5b. The seismic velocity profile created with the dispersion curves in Figure 5a. Horizontal axis is latitude; vertical axes on the left is period in seconds; on the right is approximate depths; colors are the seismic velocities. The red dots are the approximated depth to the Moho from receiver functions.

The data obtained from the calculation of the dispersion curves were stored as matrices containing latitude, longitude, velocity and initial frequency (of the frequency band). These matrices were later used to generate the surface plots shown in Figures 7, 8 and 9. All these Figures were made with the matrices corresponding to band widths of fifth of a decade intervals or periods from 10 s to 20 s for the first band, 20 s to 40 s for the second band, 40 s to 80 s for the third band, 80 s to 160 s for the fourth band. The approximate depths of these frequency bands were approximated from inversion of the model ak135 and joint inversions made for LA RISTRA [8,41,42].

- Between 10 km and 20 km approximated depth for the periods between 10 s and 20 s.
- Between 20 km and 50 km approximated depth for the periods between 20 s and 40 s.
- Between 50 km and 150 km approximated depth for the periods between 40 s and 80 s.
- Between 150 km and 350 km approximated depth for the periods between 80 s and 160 s.

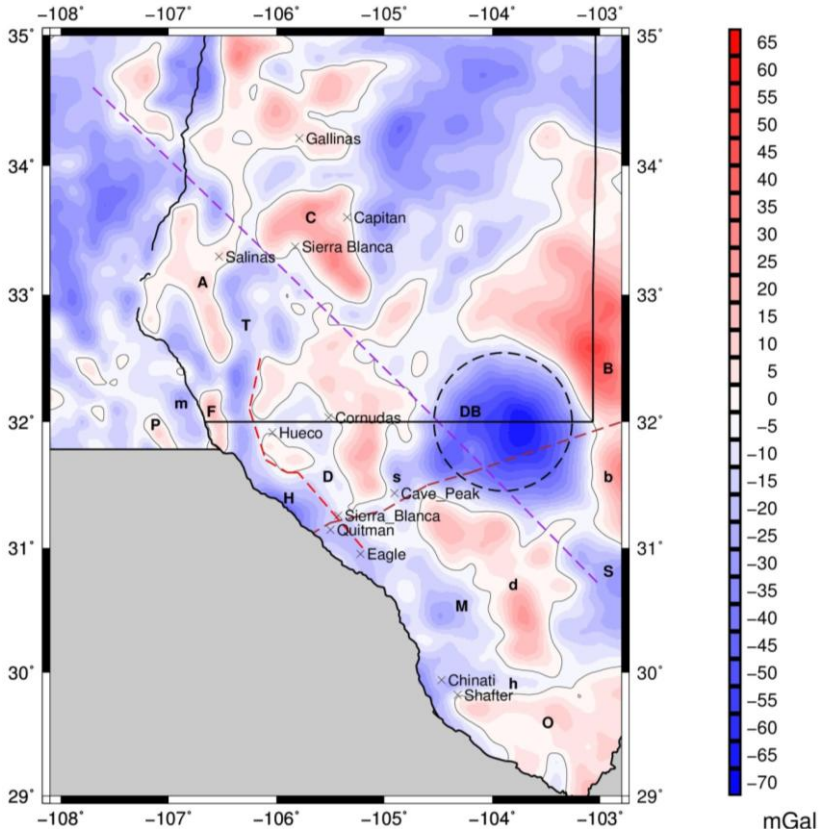

Figure 6. The isostatic residual gravity anomaly of the region. The contour lines denote the zero value of the isostatic anomaly. Some geological structures in the region are identified as: The Diablo Plateau (D), Fort Davis (d), Ouachita (O), Franklyn-Organ Mountains (F), Capitan (C), North Central Basin Platform (B), South Central Basin Platform (b), San Andres Mountains (A), Potrillos Mountains (P), Hueco Bolson (H), Delaware Basin (DB), Tularosa basin (T), Marfa basin (M), Hovey Channel (h), Mesilla basin (m), Sheffield Channel (S) and Salt basin (s). It also shows some of the tertiary REE deposits developed in the region; the dotted lines shows the boundary between Mazatzal and Grenville Precambrian provinces in brown, the alignment visible in the seismic profile for the Jalisco event in purple, the Delaware Basin in black and the Diablo Plateau west boundary in red.

Figure 6 was created to identify the geological structures that constitute this part of the North American Craton. The geological features are labeled on the top of isostatic anomaly map. The labels are:

- Stable structures identified in the region are: The Diablo Plateau (D), Fort Davis Caldera (d), Ouachita (O), Franklin-Organ Mountains (F), Capitan (C), North Central Basin Platform (B), South Central Basin Platform (b), San Andres Mountains (A) and Potrillos Mountains (P) [44].
- Some more flexible corridors surrounding these stable structures are the Hueco Bolson (H), Delaware Basin (DB), Tularosa Basin (T), Marfa Basin (M), Hovey Channel (h), Mesilla Basin (m), Sheffield Channel (S) and Salt Basin (s) [44].
- The lines shown represent the boundary between Mazatzal and Grenville Precambrian Provinces [3], the Delaware Basin, the west boundary of the Diablo Plateau and the diagonal line running from southeast to northwest passing through the center of the Delaware Basin characterizes the Jalisco event analysis. These lines are also shown in the results (Figures 7 to Figures 9) to correlate with the structures.

The results of the seismic velocity model in Figures 7 to 9 were plotted using linear Delaunay triangulation in octave [45,46], an open source alternative software of Matlab [47,48]. Figures 10 and 11 were performed for the estimation of the accuracy [49,50]. The resolution of the figures corresponds to a gridding size of 40 × 40 elements, each 1/100 of a degree in area. For the creation of the surface plot of the seismic velocities, first the Voronoi diagram was created, shown in Figure 10; then the area of interest was gridded into meshes of 5 × 5, 10 × 10, 20 × 20, 30 × 30, 40 × 40, 50 × 50 and 60 × 60 area bins and plotted using the Delaunay triangulation. Figure 11 shows the 5 × 5, 10 × 10, 40 × 40 and 60 × 60 meshes that can be compared to the Voronoi figure. The table in Figure 10 shows the number n of the n × n binning and the size of the area a of each bin. This table was created to determine the most appropriate size of the interpolation mesh; the values of the number n versus the size of the pixel as is shown in the plot next to the table.

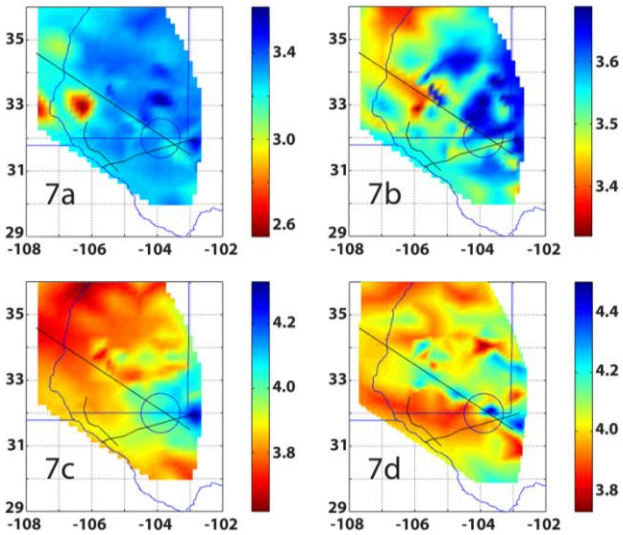

Figure 7. Images represent seismic group velocities calculated using cross correlation for the event in Jalisco. The group periods span: In 7a from 10 to 20 seconds; in 7b from 20 to 40 seconds; in 7c from 40 to 80 seconds and in 7d from 80 to 160 seconds. The x axis represents longitude, the y axis latitude and the color range is seismic velocities in km/s.

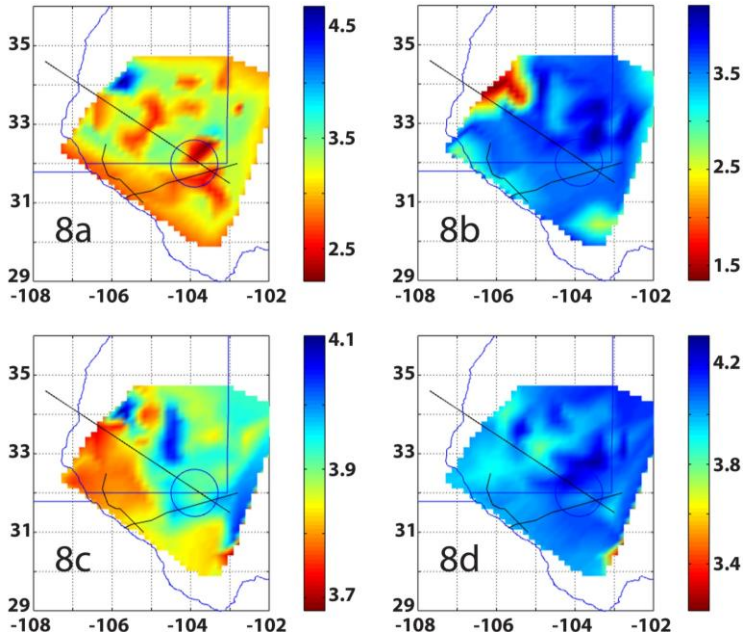

Figure 8. Images represent seismic group velocities calculated using cross correlation for the event in California. The group periods span: In 8a from 10 to 20 seconds; in 8b from 20 to 40 seconds; in 8c from 40 to 80 seconds and in 8d from 80 to 160 seconds. The x axis represents longitude, the y axis latitude and the color range is seismic velocities in km/s.

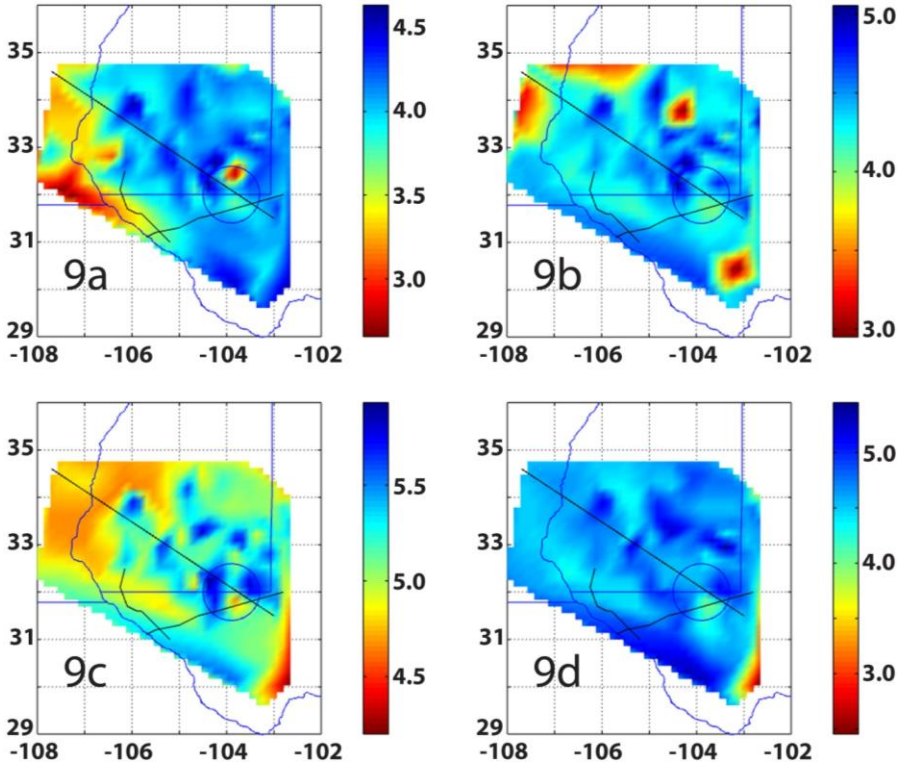

Figure 9. Images represent seismic group velocities calculated using cross correlation for the event in Samoa. The group periods span: In 9a from 10 to 20 seconds; in 9b from 20 to 40 seconds; in 9c from 40 to 80 seconds and in 9d from 80 to 160 seconds. The x axis represents longitude, the y axis latitude and the color range is seismic velocities in km/s.

4. Results and discussion

The results shown in Figures 7, 8 and 9 were chosen because their wider bandwidths enhance the effects of notches and extinction that are consequences of the multipath trajectories that characterize surface wave propagation; this effect is more frequent when using narrower frequency bandwidths [24]. As an example, in Figure 5a, there is a gap for the dispersion curve of line 3 pair 1 (l3p1); no acceptable data was available in the range between 10.00 s to 14.29 s. The gap was compensated by the blockmean interpolation algorithm of GMT that was used to generate the vertical profile in Figure 7b and by reducing the resolution between stations 223A and 123A. The choice of narrower frequency bands increases the vertical resolution but we should expect more gaps in the seismic velocity matrices due to destructive interference of the multipath effect of seismic surface wave propagation [24]. To generate the plots in Figures 7 to 9 the grid size was chosen from the analysis made in Figures 10 and 11. Figure 11 shows the unrealistic approach of using a 5 × 5 or a 10 × 10 grid in the plots and show that grids greater than 40 × 40 does not provide further information to resolve the geological structures.

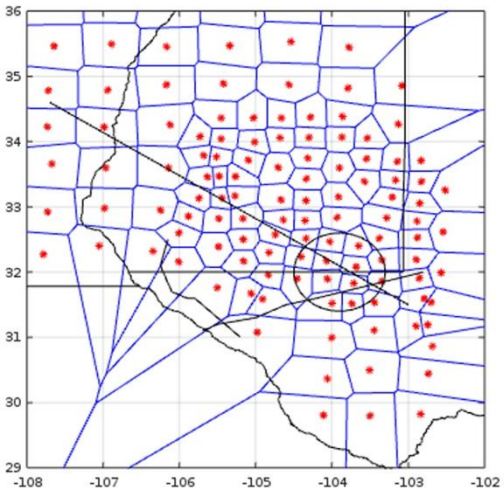

n	a
1	16.715
5	0.669
10	0.167
20	0.042
30	0.019
40	0.010
50	0.007
60	0.005

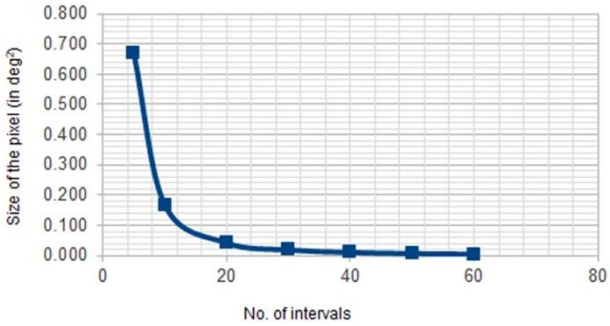

Figure 10. Voronoi diagram showing the partitioned plane for the set of positions corresponding to Rayleigh wave velocities calculated for periods ranging from 10 s to 20 s for the event in Jalisco; the table shows the number of side bins n to be calculated per side in a square array of n × n bins of area a that are shown in the plot. The size of the pixel represents a surface in units of degrees square.

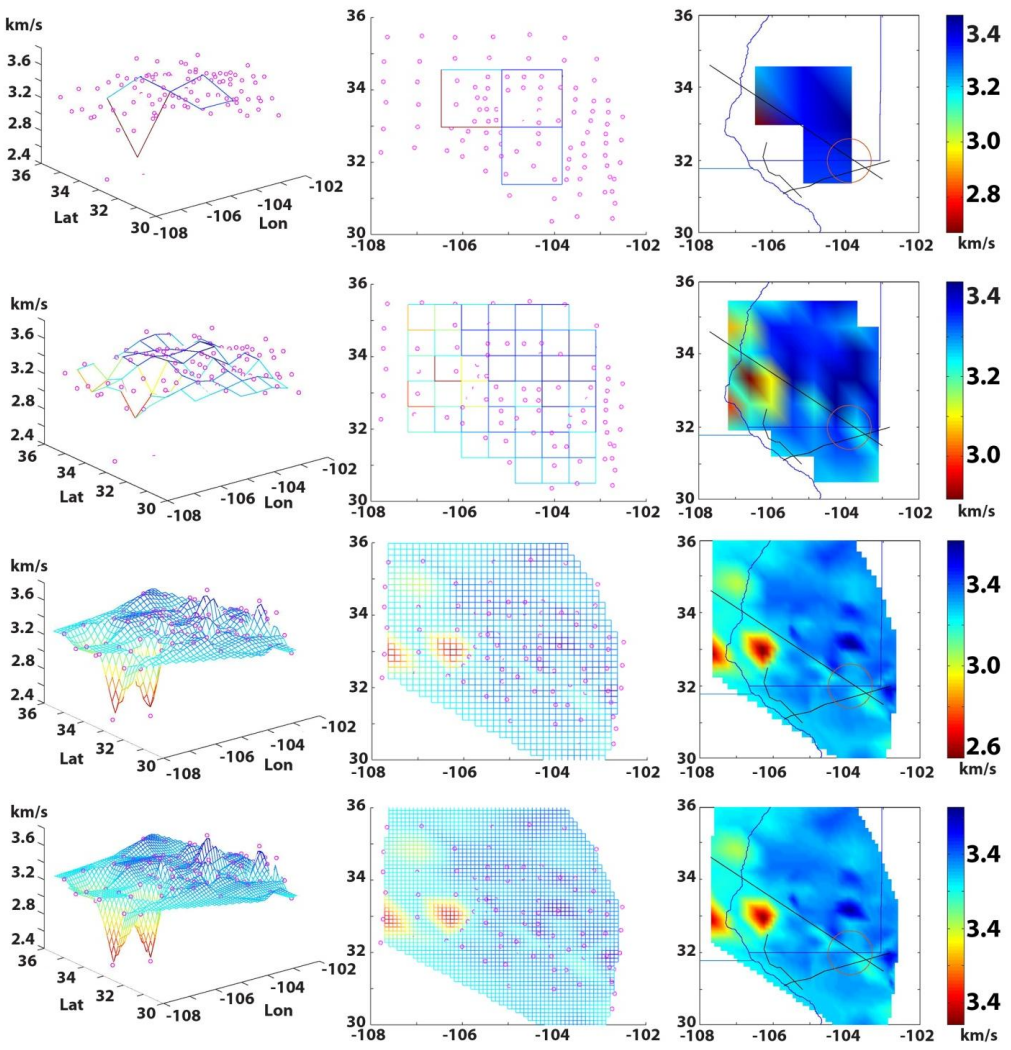

Figure 11. Plot of the 2D + 1 surface plot of the seismic velocities interpolated using Delaunay triangulation with area binned by 5 × 5, 10 × 10, 40 × 40 and 60 × 60 bins.

From the dispersion curves, Tables 1, 2, 3 and surface plots in Figures 7 to 9, the following structures were resolved: The Delaware Basin shows extreme anisotropy with complicated sub-structures that are resolved differently when the seismic velocities are calculated from sources at different distances and azimuths; its seismic velocities, ranges from 2.2 km/s up to 4.7 km/s. The seismic radiation from the event in California was the slowest, followed by that from the event in Jalisco, with the radiation from the event in Samoa being the fastest. For specific values of specific seismic velocities as function of depth and azimuth please refer to Tables 1, 2, 3. The Diablo Plateau showed seismic velocities, ranging from 3.2 km/s up to 4.3 km/s; but, for the Diablo Plateau, the seismic velocities calculated for the event in California are greater than those calculated for the event in Jalisco in opposition to the scenario in the Delaware Basin and the velocities for the event in Samoa were faster in both scenarios; the event in Jalisco resolves the seismic velocities in high correlation with the isostatic gravity anomaly, the event in Samoa somewhat and the event in California not well. The Tularosa Basin and Sheffield Channel show smaller variations in comparison with the Delaware Basin or the Diablo Plateau but still denote the anisotropy of the region; see Figures 7 to 9 and Tables 1 to 3. The area shows completely different images for every

structure depending on the azimuth of the propagation of seismic waves leading to the conclusion of high Rayleigh wave anisotropy.

Table 1. Seismic velocities for the event in Jalisco.

Approximated Rayleigh seismic wave velocities for some of the Geological Features in the area of Interest Calculated with the event in Jalisco. The seismic velocities are in kilometers per second

Geol. Feat.	Ref. Stat.	Azimuth	15±5 km Depth	35±10 km Depth	100±50 km Depth	250±100 km Depth
Tularosa Basin	Z23A	-2.4	2.4	3.3 to 3.5	3.8	3.9 to 4.3
Diablo Plateau	224A	-0.2	3.2 to 3.4	3.5 to 3.6	3.8 to 3.9	3.9
Delaware Basin	SC61	6	3.2 to 3.5	3.5 to 3.7	3.9 to 4.1	3.9 to 4.2
Fort Davis	SC61	6	3.3	3.6	3.9	4
Sheffield Channel	SC73	9	3.3	3.4	3.7	3.8

Table 2. Seismic velocities for the event in California.

Approximated Rayleigh seismic wave velocities for some of the Geological Features in the area of Interest Calculated with the event in California. The seismic velocities are in kilometers per second

Geol. Feat.	Ref. Stat.	Azimuth	15±5 km Depth	35±10 km Depth	100±50 km Depth	250±100 km Depth
Tularosa Basin	Z23A	111	2.7 to 2.9	1.3 to 1.7	3.7 to 3.8	4
Diablo Plateau	224A	113	3.2 to 3.6	3.7 to 3.5	3.8	3.9 to 4.1
Delaware Basin	SC61	110	2.2 to 3.5	3.5 to 3.7	3.9 to 4	4 to 4.3
Fort Davis	326A	113	3.2 to 3.4	3.6	3.8 to 3.9	4.1
Sheffield Channel	SC73	112	2.5 to 2.8	2.6	3.6	3.1

Table 3. Seismic velocities for the event in Samoa.

Approximated Rayleigh seismic wave velocities for some of the Geological Features in the area of Interest Calculated with the event in Samoa. The seismic velocities are in kilometers per second

Geol. Feat.	Ref. Stat.	Azimuth	15±5 km Depth	35±10 km Depth	100±50 km Depth	250±100 km Depth
Sierra Blanca NM	SC19	51	1.1	1.5	1.8	1.8
Tularosa Basin	Z23A	51	3	4.2	4.8	5 to 5.3
Diablo Plateau	224A	52	4 to 4.3	4.1 to 4.6	4.8 to 5.5	4.9 to 5.4
Delaware Basin	SC61	53	3.7 to 4.7	4.1 to 5.1	4.6 to 6	4.5 to 4.7
Fort Davis	426A	54	4.1 to 4.2	4.2 to 4.4	5.1	5.1 to 5.9
Sheffield Channel	SC73	54	3.9	2.8	4.9	4.9

5. Conclusions

The use of Rayleigh wave cross correlation analysis is a good tool to identify geological structures of regional size in the crust and upper mantle if the vertical broad band (BHZ) seismic data

is available. For this work, data was provided by TA and Flex arrays [19,20].

If you are planning to use Rayleigh wave cross correlation it is not recommended to combine the data from different events for the following reasons:

- The results of the seismic velocity calculations for different events have different averages and standard deviations. The contrast of the plot is affected by the standard deviation.
- Anisotropy causes huge differences in seismic velocities for surface waves travelling along different azimuths in a specific region. The seismic velocity of a region is a function of the angle of incidence of the seismic radiation.
- The uniqueness of the alignment in the strike and slip of the event (focal mechanism) produces specific distribution of stresses; it is elucidated by the moment tensor [51]. The geology reacts differently to different events.

For these reasons the plot performed for different events leads to completely different images. From observation of the results, the structures are best resolved by radiation patterns that are perpendicular to their boundaries.

- Surface waves have some disadvantages.
- Extinction when passing through any geological structure with content of liquid or melts. This effect is caused because shear waves do not propagate in liquids; then, melting, partial melting or content of fluid in the geological formation along the path can cause anomalous correlation or extinction. In this area we have this effect when seismic waves pass through the Mogollon-Datil volcanic field; due to this problem the area near the upper Rio Grande Rift is not possible to model for events like California or Jalisco.
- Another important problem arising from surface wave propagation is called multi-pathing; this problem can be understood better if we recall the Huygens-Fresnel's wave propagation principle instead of the ray tracing model [24,51]. Correlation between two stations that, according to ray tracing, follow similar paths due to the presence of nearby boundaries striking along the propagation with large differences in seismic velocities, leads to negative time correlations. In other words, if signals arriving in the first station came from nearby geological structures with faster seismic speed than that of the second station, then the time correlation leads to negative values. This can be seen as the gap in the dispersion curves shown for the Jalisco event in Figure 5a.
- In another scenario the difference in phase between the two paths superposes destructively causing extinction of the amplitude in the correlation. The reduction or lack of amplitudes in the signal is seen in the dispersion as a discontinuity commonly called notch; the presence of notches causes loss of resolution in the plot [24].

For the area of this investigation, the plot has lower resolution on the rift than on the plains (in the shoulder of the rift also called flank). For this reason, we decided to use the widest bandwidths to perform the plot shown in Figures 9 to 11.

Acknowledgments

The data used in this study were provided by Incorporated Research Institutions for Seismology Data Management Center (IRIS DMC), United States Geological Survey (USGS), National Oceanic and Atmospheric Administration's National Centers for Environmental Information (NOAA's NCEI) and General Mopping Tools (GMT).

Conflict of interest

All authors declare no conflicts of interest in this paper.

Appendix

Appendix 1. List of stations for network TA.

NETWORK	STATION	LAT	LON	NETWORK	STATION	LAT	LON
TA	121A	32.5324	−107.7851	TA	TASL	34.9454	−106.4565
TA	122A	32.6995	−107.0005	TA	TASM	34.9455	−106.46
TA	123A	32.6349	−106.2622	TA	TASN	34.9455	−106.46
TA	124A	32.7001	−105.4544	TA	TASO	34.9455	−106.46
TA	125A	32.6588	−104.6573	TA	TASP	34.9455	−106.46
TA	126A	32.6462	−104.0204	TA	TVZX	34.0733	−106.9196
TA	127A	32.6764	−103.3575	TA	X21A	34.4457	−107.7857
TA	128A	32.6213	−102.485	TA	X22A	34.5058	−107.0102
TA	221A	32.0094	−107.7782	TA	X23A	34.581	−106.1881
TA	222A	32.1046	−107.1013	TA	X24A	34.5646	−105.4349
TA	223A	32.0062	−106.4276	TA	X25A	34.5271	−104.6621
TA	224A	32.076	−105.5226	TA	X26A	34.5508	−103.8103
TA	225A	32.1101	−104.8229	TA	X27A	34.6469	−103.0974
TA	226A	32.0618	−104.1014	TA	X28A	34.5185	−102.1973
TA	226B	32.0778	−104.1654	TA	Y21A	34.0087	−107.674
TA	227A	32.012	−103.2924	TA	Y22A	33.937	−106.9652
TA	228A	32.118	−102.5918	TA	Y22C	34.0741	−106.9211
TA	324A	31.4425	−105.4828	TA	Y22D	34.0739	−106.921
TA	325A	31.3711	−104.9712	TA	Y22E	34.0742	−106.9208
TA	326A	31.3165	−103.9786	TA	Y22F	34.0741	−106.9209
TA	327A	31.3691	−103.4923	TA	Y23A	33.9315	−106.0549
TA	328A	31.3818	−102.8097	TA	Y24A	33.9257	−105.4361
TA	425A	30.7862	−104.9857	TA	Y25A	33.9229	−104.6928
TA	426A	30.6689	−104.0293	TA	Y26A	33.9232	−103.8246
TA	427A	30.8498	−103.4018	TA	Y27A	33.8839	−103.1633
TA	428A	30.7263	−102.6847	TA	Y28A	33.9086	−102.2479
TA	526A	30.0609	−104.0898	TA	Z21A	33.3086	−107.6712
TA	527A	30.1456	−103.6119	TA	Z22A	33.2555	−106.9639
TA	528A	30.1615	−102.788	TA	Z23A	33.2621	−106.2319
TA	529A	30.1246	−102.2204	TA	Z24A	33.3298	−105.3649
TA	626A	29.554	−104.1335	TA	Z25A	33.2797	−104.7171
TA	627A	29.4528	−103.3887	TA	Z26A	33.2716	−103.9798
TA	628A	29.4862	−102.8885	TA	Z27A	33.315	−103.2145
TA	MSTX	33.9696	−102.7724	TA	Z28A	33.2884	−102.3866

Appendix 2. List of stations for network XR.

NETWORK	STATION	LAT	LON	NETWORK	STATION	LAT	LON
XR	SC04	34.5228	−105.8119	XR	SC40	32.9317	−103.54
XR	SC05	34.5715	−105.0554	XR	SC41	32.9833	−103.2056
XR	SC06	34.5145	−104.2664	XR	SC42	32.8728	−102.8612
XR	SC07	34.1838	−105.6877	XR	SC43	32.9426	−102.5369
XR	SC08	34.1567	−105.4697	XR	SC44	32.7572	−105.947
XR	SC09	34.1517	−105.0013	XR	SC45	32.6337	−105.1552
XR	SC10	34.1937	−104.6666	XR	SC46	32.654	−104.3614
XR	SC11	34.2323	−104.2959	XR	SC47	32.629	−103.6257
XR	SC12	34.2148	−103.9116	XR	SC48	32.6899	−102.905
XR	SC13	34.2135	−103.5269	XR	SC49	32.443	−106.064
XR	SC14	33.9682	−105.7695	XR	SC50	32.3895	−105.6153
XR	SC15	33.8308	−105.0255	XR	SC51	32.3673	−105.1718
XR	SC16	33.8903	−104.3043	XR	SC52	32.488	−104.8272
XR	SC17	33.893	−103.5446	XR	SC53	32.3766	−104.3192
XR	SC18	33.8774	−102.8409	XR	SC54	32.2837	−104.0398
XR	SC19	33.5188	−105.9744	XR	SC55	32.1712	−103.6733
XR	SC20	33.6042	−105.5935	XR	SC56	32.3554	−103.3986
XR	SC21	33.5975	−105.1655	XR	SC57	32.3691	−102.8513
XR	SC22	33.5682	−104.7542	XR	SC58	32.2888	−102.5482
XR	SC23	33.5995	−104.3282	XR	SC59	31.9694	−105.1481
XR	SC25	33.5806	−103.5482	XR	SC60	32.0937	−104.4877
XR	SC26	33.5044	−103.1184	XR	SC61	31.9895	−103.6911
XR	SC27	33.5385	−102.8207	XR	SC62	32.0119	−102.9373
XR	SC28	33.5662	−102.4915	XR	SC63	31.8029	−104.8464
XR	SC29	33.3102	−105.6705	XR	SC64	31.6996	−104.4258
XR	SC30	33.2738	−105.17	XR	SC65	31.727	−104.0178
XR	SC31	33.259	−104.3415	XR	SC66	31.6679	−103.7363
XR	SC32	33.1939	−103.5979	XR	SC67	31.7051	−103.3951
XR	SC33	33.2334	−102.8343	XR	SC68	31.8027	−102.77
XR	SC34	32.9513	−105.8163	XR	SC69	31.6905	−102.588
XR	SC35	32.9369	−105.5153	XR	SC70	31.3663	−103.7374
XR	SC36	33.0053	−105.18	XR	SC71	31.6463	−103.0655
XR	SC37	32.937	−104.6192	XR	SC72	31.1096	−103.6346
XR	SC38	32.9288	−104.3402	XR	SC73	30.9611	−102.9875
XR	SC39	33.0286	−103.8453	XR	SC74	31.0024	−102.6771
				XR	SC75	31.8742	−105.952

References

1. Whitmeyer SJ, Karlstrom KE (2007) Tectonic model for the Proterozoic growth of North America. *Geosphere* 3: 220–259.
2. Yuan H, Romanowicz B (2010) Lithospheric layering in the North American craton. *Nature* 466: 1063–1068.
3. Karlstrom KE, Amato JM, Williams ML, et al. (2004) Proterozoic Tectonic Evolution of the New Mexico Region: A Synthesis, In: Mack GH, Giles CA, *The Geology of New Mexico, A Geologic History*, 1 Ed., NMGS, 389–406.
4. Davison DD, (1980) Precambrian geology of the Van Horn area, Texas, In: Dickerson PW, Hoffer JM, Callender JF, *Trans Pecos Region (West Texas), New Mexico Geological Society 31st Annual Fall Field Conference Guidebook*, 308: 151–154.
5. Mosher S, Hoh AM, Zumbro JA, et al. (2004) Tectonic evolution of the eastern Llano uplift, central Texas: A record of Grenville orogenesis along the southern Laurentian margin. *Mem Geol Sic Am* 197: 783–798.
6. Pulliam J, Grand SP, Xia Y, et al. (2010) Edge-Driven Convection Beneath the Rio Grande Rift, *InSights the EarthScope. Summer 2010*: 2.
7. Gök R, Ni JF, West M, et al. (2003) Shear wave splitting and mantle flow beneath LA RISTRA. *Geophys Res Lett* 30: 16.
8. West M, Ni J, Baldridge WS, et al. (2004) Crust and upper mantle shear wave structure of the Southwest United States: Implications for rifting and support for high elevation. *J Geophys Res* 109: 1–16.
9. Shen W, Ritzwoller MH, Schulte-Pelkum V (2013) A 3-D model of the crust and uppermost mantle beneath the Central and Western US by joint inversion of receiver functions and surface wave dispersion. *J Geophys Res Solid Earth* 118: 262–276.
10. Bryan S (2007) Silicic large igneous provinces. *Episodes* 30: 20–31.
11. Goodell PC, Mahar MA, Mickus KL, et al. (2017) The presence of a stable "Megablock" in the southwestern North American Proterozoic craton in northern Mexico. *Precambrian Res* 300: 273–288.
12. Warner LA, Holser WT, Wilmarth VR, et al. (1959) Occurrence of nonpegmatite beryllium in the United States. *Geol Surv Prof Pap 318*.
13. Aguirre-díaz GJ, Labarthe-hernández G (2003) Fissure ignimbrites: Fissure-source origin for voluminous ignimbrites of the Sierra Madre Occidental and its relationship with Basin and Range faulting. *Geology* 31: 773–776.
14. Ferrari L, López-Martínez M, Rosas-Elguera J (2002) Ignimbrite flare-up and deformation in the southern Sierra Madre Occidental, western Mexico: Implications for the late subduction history of the Farallon Plate. *Tectonics* 21: 1–23.
15. James EW, Henry CD (1991) Compositional changes in Trans-Pecos Texas Magmatism Coincident with Cenozoic stress realignment. *J Geophys Res Solid Earth* 96: 13561–13575.
16. McLemore VT, North RM, Leppert S, (1988) Rare-earth elements (REE), niobium and thorium districts and occurrences. In: *New Mexico: New Mexico Bureau of Mines and Mineral Resources, Open-file Report OF-324*, 1–28.
17. Dunbar NW, Campbell AR, Candela PA (1996) Physical, chemical, and mineralogical evidence for magmatic fluid migration within the Capitan pluton, southeastern New Mexico. *Geol Soc*

Am Bull 108: 318–333.
18. Gibson SA, Thompson RN, Leat PT, et al. (1993) Ultrapotassic Magmas along the Flanks of the Oligo-Miocene Rio Grande Rift, USA: Monitors of the zone of lithospheric mantle extensional and thinning beneath a continental rift. *J Petrol* 34: 187–228.
19. TA, Transportable Seismic Network: Imaging the Earth's Interior. Available from: http://www.usarray.org/researchers/obs/transportable.
20. SIEDCAR, Seismic Investigation of Edge Driven Convection Associated with The Rio Grande Rift. Flex Array. Available from: http://www.usarray.org/researchers/obs/flexible/deployments/siedcar/.
21. Meltzer A, Rudnick R, Zeitler P, et al. (1999) The USArray Initiative. *Geol Soc Am Today* 9: 8–10.
22. IRIS, Incorporated Research Institutions for Seismology. Available from: http://ds.iris.edu/ds/.
23. Wilber 3, IRIS Wilber 3: Select Event. Available from: http://ds.iris.edu/wilber3/find_event.
24. Ammon CJ (2001) Notes on Seismic Surface-Wave Processing. Part I. Group Velocity Estimation, Saint Louis University. Ver 3.9.0. Surface Wave Multiple Filter Analysis Software Documents. Available from: http://eqseis.geosc.psu.edu/~cammon/.
25. Singh AP, Mishra OP, Rastogi BK (2012) A new insight into crustal heterogeneity beneath the 2001 Bhuj earthquake region of northwest India and its implications for rupture initiations. *J Asian Earth Sci* 48: 31–42.
26. Dixit M, Singh AP, Mishra OP (2017) Rayleigh wave group velocity tomography of Gujarat region, Western India and its implications to mantle dynamics. *J Seismol* 21: 1–15.
27. USGS, United States Geological Survey, Mineral Resources On-Line Spatial Data. Available from: https://mrdata.usgs.gov/gravity/isostatic/.
28. Paterson NR, Reeves CV (1985) Applications of gravity and magnetic surveys; the state-of-the-art. *Geophysics* 50: 2558–2594.
29. Phillips JD, Duval JS, Ambroziak RA (1993) National geophysical data grids; gamma-ray, gravity, magnetic, and topographic data for the conterminous United States. *Data*.
30. Wessel P, Smith WHF (1996) A global, self-consistent, hierarchical, high-resolution shoreline database. *J Geophys Res Solid Earth* 101: 8741–8743.
31. Wessel P, Smith WHF, Scharroo R, et al. (2013) Generic Mapping Tools: Improved version released. *EOS Trans Am Geophys Union* 94: 409–410.
32. NOAA's NCEI, National Oceanic and Atmospheric Administration's National Centers for Environmental Information. Available from: https://www.ngdc.noaa.gov/mgg/global/.
33. Dean EA, Keller GR (1991) Interactive processing to obtain interstation surface-wave dispersion. *AAPS J* 4451: 1–6.
34. Kovach RL (1978) Seismic surface waves and crustal and upper mantle structure. *Rev Geophys* 16: 1–13.
35. Dziewonski A, Bloch S, Landisman M (1969) A technique for the analysis of transient seismic signals. *Bull Seism Soc Am* 59: 427–444.
36. Herrin E, Goforth T (1977) Phase-matched filters: Application to the study of Rayleigh waves. *Bull Seism Soc Am* 67: 1259–1275.
37. SAC, Seismic Analysis Code. Available from: https://ds.iris.edu/ds/nodes/dmc/software/downloads/sac/.
38. Helffrich G, Wookey J, Bastow I (2013) The Seismic Analysis Code. In: *A Primer and User's Guide*, 1 Ed., Cambridge University Press.
39. Butterworth S (1929) On the theory of filter amplifiers. *Wireless Engineer*.
40. Bianchi G (2007) Electronic filter simulation & design. *Amacom*.

41. Kennett BLN, Engdahl ER, Buland R (1995) Constraints on seismic velocities in the Earth from travel times. *Geophys J Int* 122: 108–124.
42. Ward KM (2015) Ambient noise tomography across the southern Alaskan Cordillera. *Geophys Res Lett* 42: 3218–3227.
43. EARS, The EarthScope Automated Receiver Survey. Available from: http://ears.iris.washington.edu/.
44. Ewing TE (1991) The Tectonic framework of Texas: Text to accompany "The Tectonic map of Texas", In: *Bureau of Economic Geology*, Publication SM0001: 1–36.
45. GNU Octave. Scientific Programing Language. Available from: https://www.gnu.org/software/octave/.
46. Hansen JS (2011) GNU Octave Beginner's Guide. *Packt Publishing Ltd*.
47. Hanselman D, Littefield B (1998) Mastering Matlab 5. Prentice *Hall Inc*.
48. MathWorks Documentation. Available from: https://www.mathworks.com/help/.
49. Holzbecher E, Si H (2008) Accuracy Test for COMSOL -and Delaunay Meshes. *Excerpt from the Proceedings of the COMSOL Conference 2008 Hanover*.
50. Jänicke L, Kost A (1996) Error estimation and adaptive mesh generation in the 2D and 3D finite element method. *IEEE Trans Magn* 32: 1334–1337.
51. Stein S, Wysession M, (2002) An introduction to seismology, In: *Earthquakes and Earth Structure*, 1 Ed., Blackwell Pub.

AIMS Press